A Complex Domain Mapping of the SCN for an Effective PML Implementation in TLM

Jomiloju S. Odeyemi, Ana Vukovic, *Member,* IEEE, Trevor M. Benson and Phillip D. Sewell

Abstract— **An improved implementation of the perfectly matched layer (PML) is developed for the Transmission Line Modelling (TLM) method based on a mapping of the symmetrical condensed node (SCN) to an analytically extended geometric space. By mapping the TLM node, a medium – circuit equivalence is developed which maps transmission line parameters from real to complex domain. This consequently modifies the TLM scatter-connect process. The PML implementation is demonstrated for canonical cases where it is shown to have a comparable absorption performance and a significantly improved temporal stability relative to previously published TLM-PML formulations.**

Index Terms— **Perfectly matched layer, stability, stretched-coordinate, transmission line modelling, symmetrical condensed node.**

I. INTRODUCTION

THE Transmission Line Modelling (TLM) method is a powerful time-domain numerical technique with a demonstrated success for simulating complex electromagnetic problems [1]-[3]. Its formulation is developed based upon mapping Maxwell's equations to a network of transmission lines equations which results in an unconditionally stable algorithm [1]-[2]. In the case of open boundary problems, it is critically important for the viability of large-scale computations to minimize the volume of free space that needs to be explicitly modelled. Therefore, the computational domain is terminated with either a matched boundary, an absorbing boundary condition (ABC) [4]-[5] or Perfectly Matched Layer (PML) [6]-[12]. Of these three, the PML demonstrates a superior absorption performance over a wider frequency range and for wider angles of incidence.

The PML was initially proposed by Bérenger through a split-field formulation and was implemented in the Finite Difference Time Domain (FDTD) method [13] as an artificial absorbing medium introduced at the edges of the computational domain. The key attraction of the PML is the impedance matching feature which results in a theoretical reflection free outward propagation. Therefore, by an appropriate choice of the PML's conductivity a sufficiently fast decay of the outgoing solutions can be enforced such that the solutions practically vanishes upon arrival at the PML outer boundary.

Due to the relative ease of implementation of FDTD algorithms, numerous PML schemes and extensions have followed Bérenger's original development. In sharp contrast, only a handful of PML formulations in three-dimensional (3D) TLM have been demonstrated, all of which have implemented the PML theory by directly modifying the field behavior at the TLM node centers [6]-[11]. A development based on a coupling between the TLM-FDTD network pioneered the PML implementation for 3D TLM simulations [7]. This offered the advantage of providing unconditional stability but suffered from a degradation in its absorption performance due to the non-physical reflections generated at the non-uniform TLM-FDTD interface. A number of pure TLM developments have since been proposed and demonstrated for the TLM symmetrical condensed node (SCN). The initial development was proposed in [8] which implemented the PML by splitting each field component into subcomponents and applying anisotropic electric/magnetic conductivities to attenuate along each direction of propagation. The process of field splitting resulted in an increase in total voltage stored per node. A second split-field based SCN-PML was developed in [9] which employed a direct discretization implementation through a centered differencing and averaging of the PML equations. This demonstrated similar absorption performance to [8] and had the advantage of requiring less storage per node. A limitation with the formulation proposed in [9] however is the singularities that arise in the inductive stubs which prevent operation at the maximum time step permitted. The singularity issues reported in [9] was addressed in [10] by an extension which enabled operation at the maximum time step. The formulation proposed in [10] also introduced a damping factor to attenuate evanescent fields and this was shown to improve the temporal behavior by delaying the occurrence of instabilities. Nonetheless, due to the inherent limitation of the split-field PML theory the formulations proposed in [8]-[10] are less suitable to applications involving lossy media. Results from a stretched coordinate based (SCB) SCN-PML node have been demonstrated for terminating canonical waveguide structures [11]. This employed the use of the Z-transform to impose the frequency dependent stretch variables [14] on the fields of the SCN node. The absorption behavior was shown to yield comparable results with previous SCN-PML schemes, however, a clear disadvantage with this implementation is the instabilities which arise, also the extension to the termination of non-waveguide structures is not clear.

Whilst all SCN-PML implementations have demonstrated some success, and show a good agreement in their absorption performance, they also exhibit a weak temporal stability, which in some cases generate in exponentially growing solutions in the problem domain [8]-[11]. This degrading phenomenon is practically unacceptable and its removal is a prime motivator of this work.

In this paper, we extend the mapping approach, briefly described in [12], to the full 3D TLM case for the first time. The SCN variant of the 3D TLM is considered, due to its simplicity and popularity in practice [1]-[2]. To emphasize, the PML theory presented here is implemented as a modification of the transmission line parameters as opposed to the node scattering characteristics demonstrated in previous schemes [8]-[11]. This approach to PML implementation is particularly distinct to the formulation published in [11] which introduces the stretched coordinate PML theory as a correction of fields. By employing a mapping approach, a direct discretization of the PML equations is avoided which, in a similar fashion to the classical TLM development, ensures an unconditionally stable algorithm.

The remainder of the paper is organized as follows. In Section II a direct mapping is established between Maxwell's equations in the stretched coordinate space and the transmission line parameters of the SCN. We refer to this implementation as the mapped SCN-PML. Modified scatter-connect equations due to the mapping are subsequently derived. For simplicity, the scatter equations are derived for the stub free SCN. Section III outlines the full 3D implementation for the mapped SCN-PML formulation. In section IV, the validity of the mapped SCN-PML is demonstrated by comparing its absorption performance and stability against the PML formulations proposed in [9] and [10]. Section V outlines the main conclusions of the paper.

II. THE FORMULATION

In this section, the mapping of the Maxwell's equations in the stretched coordinate space to the transmission line parameters of the SCN is derived. The TLM scatter-connect equations for the SCN in the stretched coordinate space are subsequently derived.

The schematic of the SCN is shown in Fig.1 which describes a block of space with dimensions given as $\Delta x \times \Delta y \times \Delta z$ and material properties $\mu = \mu_r \mu_0$ and $\epsilon = \epsilon_r \epsilon_0$. This model accounts for all three coordinate directions and field polarizations in a 3D geometry. The SCN algorithm introduces 12 voltages in the form of $V_{i\alpha j}$, where i represents the direction and j the polarization of the line ($i, j \in \{x, y, z\}$ and $i \neq j$) and $\alpha \in \{n, p\}$ indicates the position of the line on the negative (n) or positive (p) side relative to the origin of coordinates at the center of the node. Each i-directed transmission arm supports the propagation of a pair of j and k-polarized fields. Therefore, there is an associated pair of characteristic impedances Z_{ij}, Z_{ik}, along each arm, which results in a total of 12 characteristic impedances per node.

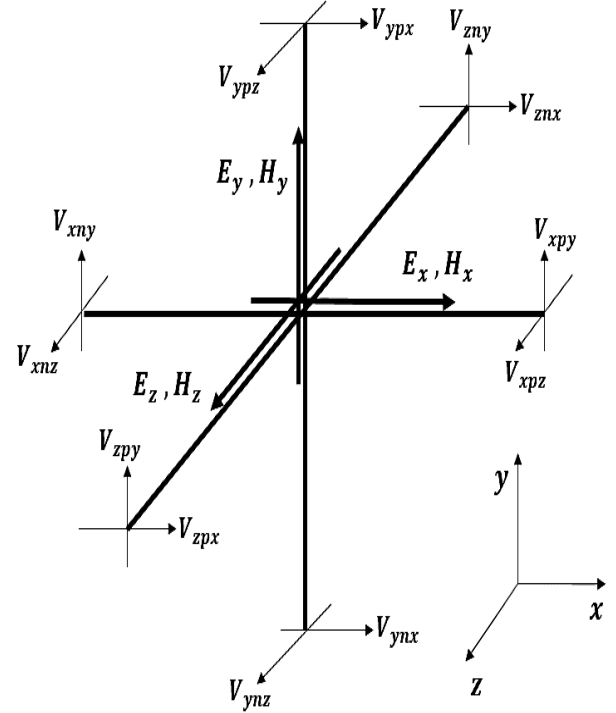Consider the y-projections of Faraday's and Ampere's laws given in a coordinate stretched space as

Fig. 1. Topology of the Symmetrical Condensed Node (SCN) showing the directions and polarizations of the transmission lines.

$$\frac{1}{S_z}\frac{\partial E_x}{\partial z} - \frac{1}{S_x}\frac{\partial E_z}{\partial x} = -\mu_y\frac{\partial H_y}{\partial t} - \sigma_{my}H_y \qquad (1)$$

$$\frac{1}{S_z}\frac{\partial H_x}{\partial z} - \frac{1}{S_x}\frac{\partial H_z}{\partial x} = \epsilon_y\frac{\partial E_y}{\partial t} + \sigma_{ey}E_y, \qquad (2)$$

where μ_y and ϵ_y denote the permeability and permittivity, and σ_{my} and σ_{ey} are the magnetic and electric conductivity of the medium and S_x, S_y and S_z are coordinate stretch factors in x-, y- and z- directions which are compactly expressed as

$$S_i = 1 + \frac{\sigma_{si}}{j\omega}, \qquad \sigma_{si}(i) = \frac{\sigma_i}{\epsilon_0} \geq 0, i = x, y, z \qquad (3)$$

where σ_i represents the electric conductivity profile along the i-coordinate axis that controls the rate of decay. The coordinate stretch factors employed in (1) and (2) theoretically support the desired reflection-free attenuation of propagating waves and are defined according to stretched coordinate PML [14].

By multiplying both sides of (1) and (2) with $S_z S_x$ the following results are obtained,

$$S_x\frac{\partial E_x}{\partial z} - S_z\frac{\partial E_z}{\partial x} = -\frac{S_z S_x}{S_y}\mu_y\frac{S_y\partial H_y}{\partial t} - \frac{S_z S_x}{S_y}\sigma_{my}H_y S_y \quad (4)$$

$$S_x\frac{\partial H_x}{\partial z} - S_z\frac{\partial H_z}{\partial x} = \frac{S_z S_x}{S_y}\epsilon_y\frac{S_y\partial E_y}{\partial t} + \frac{S_z S_x}{S_y}\sigma_{ey}E_y S_y. \quad (5)$$

Equations (4) and (5) are a re-expression of (1) and (2) and represent Maxwell's equations in the coordinate stretched space. The form adopted highlights the transformation of the medium parameters which are given as

$$\tilde{\mu}_y = \frac{S_z S_x}{S_y}\mu_y, \qquad \tilde{\epsilon}_y = \frac{S_z S_x}{S_y}\epsilon_y$$

$$\tilde{\sigma}_{my} = \frac{S_z S_x}{S_y}\sigma_{my}, \qquad \tilde{\sigma}_{ey} = \frac{S_z S_x}{S_y}\sigma_{ey}$$

where the $\sim$ indicates parameters in the complex stretched space. Such a transformation of the medium parameters reveals the geometry and material inter-relationship of Maxwell's equations which enables the form invariance property [15] where the solutions in a stretched coordinate space with free space material parameters are the same as solutions in an unstretched space but with more complex anisotropic material parameters. This interpretation is crucial to our TLM-PML development since, according to the underlying TLM medium-circuit equivalence, the coordinate stretching is thus applied directly to the numerical algorithm. Therefore, by a mapping of the TLM circuit parameters, the TLM solutions to Maxwell's equations is obtained but with the desired absorption behavior applied.

According to the TLM medium-to-circuit equivalence [1]-[2], the SCN circuit parameters in the stretched space are now

$$\tilde{L}_y^t = \tilde{\mu}_y \Delta l = \frac{S_z S_x}{S_y}\mu_y \Delta l$$

$$\tilde{C}_y^t = \tilde{\epsilon}_y \Delta l = \frac{S_z S_x}{S_y}\epsilon_y \Delta l$$

$$\tilde{R}_y = \tilde{\sigma}_{my}\Delta l = \frac{S_z S_x}{S_y}\sigma_{my}\Delta l$$

$$\tilde{G}_y = \tilde{\sigma}_{ey}\Delta l = \frac{S_z S_x}{S_y}\sigma_{ey}\Delta l \qquad (6)$$

with

$$\Delta l = \frac{\Delta_z \Delta_x}{\Delta_y},$$

where $\tilde{L}_y^t$ and $\tilde{C}_y^t$ represent the total inductance and capacitance along the y-direction, respectively, and $\tilde{R}_y$ and $\tilde{G}_y$ represent the resistance and conductance along the y-directions, respectively. The total inductance $\tilde{L}_j^t$ and capacitance $\tilde{C}_j^t$ in the mapped SCN-PML are comprised of the sum of the contributions from each i-directed and j-polarized distributed inductance and capacitance $\tilde{L}_{ij}$ and $\tilde{C}_{ij}$ respectively, as well as the inductive and capacitive stubs $\tilde{L}_j^s$ and $\tilde{C}_j^o$, respectively [16]. The general constitutive relations in the mapped SCN-PML are therefore given as

$$\tilde{L}_j^t = \tilde{L}_{ik}\Delta i + \tilde{L}_{ki}\Delta k + \tilde{L}_j^s$$

$$\tilde{C}_j^t = \tilde{C}_{ij}\,\Delta i + \tilde{C}_{kj}\Delta k + \tilde{C}_j^o. \qquad (7)$$

Each distributed inductance and capacitance in (7) undergoes a similar stretching as the corresponding L_j^t and C_j^t (6) which yields the following relations

$$\tilde{L}_{ik} = \frac{S_i S_k}{S_j}L_{ik}, \qquad \tilde{L}_j^s = \frac{S_i S_k}{S_j}L_j^s$$

$$\tilde{C}_{ij} = \frac{S_i S_k}{S_j}C_{ij}, \qquad \tilde{C}_j^o = \frac{S_i S_k}{S_j}C_o^{\,j}. \qquad (8)$$

Following from (8), the propagation delay $\widetilde{\Delta t_i}$ experienced by pulses propagating along the i-directed TLs is given by

$$\widetilde{\Delta t_i} = \Delta i \sqrt{\tilde{L}_{ij}\tilde{C}_{ij}} = \Delta i \sqrt{\frac{S_i S_j}{S_k}L_{ij}\,\frac{S_i S_k}{S_j}C_{ij}} = S_i \Delta t_i$$

$$= \Delta t_i + j\left(\frac{\Delta t_i \sigma_{si}}{j\omega}\right) \qquad (9)$$

and the characteristic impedance (admittance) of the i-directed and j-polarized TLs in the mapped SCN-PML is given as

$$\tilde{Z}_{ij} = \sqrt{\frac{\frac{S_i S_j}{S_k}L_{ij}}{\frac{S_i S_k}{S_j}C_{ij}}} = \frac{S_j}{S_k}Z_{ij} = \frac{1}{\tilde{Y}_{ij}} \qquad (10)$$

The characteristic impedance/admittance of the stub lines experience a similar stretching to the corresponding L_j^s and $C_o^{\,j}$ parameters. Therefore, the transformed impedance of the short-circuit stub is given as

$$\tilde{Z}_{sj} = Z_{sj}\frac{S_i S_k}{S_j}, \qquad (11)$$

and the transformed admittance open-circuit stub is given as

$$\tilde{Y}_{oj} = Y_{oj}\frac{S_i S_k}{S_j}. \qquad (12)$$

A. *TLM Scatter-Connect in the mapped SCN-PML*

In this sub-section an equivalent network model approach [17]-[18] is employed to derive the scatter equations of the mapped SCN-PML.

The evolution of the field in TLM follows the well-known scatter-connect algorithm, [2], whereby at each time step incident voltage pulses $V_{i\alpha j}^i$ scatter at the node center and result into reflected voltage pulses $V_{i\alpha j}^r$ which subsequently become the incident voltage pulse on the neighboring nodes at the next time step.

The 2D Thèvenin circuits analogous to (4) and (5), which permit solution of the mapped SCN-PML nodal scattering, are illustrated in Fig. 2 and Fig. 3, respectively. Both circuits follow the standard form of 2D Thèvenin circuits [2] but employ mapped characteristic impedances given by (10). Therefore, an expression for the equivalent voltage in the j direction $\tilde{V}_j$ can be easily obtained by applying circuit theory to the mapped shunt circuit (Fig.2) to give

4

$$\tilde{V}_j = 2\frac{S_kY_{ij}\left(V^i_{inj}+V^i_{ipj}\right)+S_iY_{kj}(V^i_{kpj}+V^i_{knj})+S_iS_kY_{oj}V^i_{oj}}{2S_kY_{ij}+2S_iY_{kj}+S_iS_k(G_{ej}+Y_{oj})}$$

(13)

Similarly, an expression for the equivalent current in the k direction $\tilde{I}_k$ is obtained from Fig.3 as

$$\tilde{I}_k = 2\frac{\left(V^i_{inj}-V^i_{ipj}\right)+\left(V^i_{jpi}-V^i_{jni}\right)-V^i_{sk}}{\frac{S_j}{S_k}Z_{ij}+\frac{S_i}{S_k}Z_{ji}+\frac{S_iS_j}{S_k}(Z_{sk}+R_{mk})}.$$

(14)

Overall, the scattering procedure in the mapped SCN-PML can be written as [17]-[18]

$$V^r_{inj} = \tilde{V}_j \pm \tilde{I}_k\tilde{Z}_{ij} - V^i_{ipj}$$

$$V^r_{ipj} = \tilde{V}_j \mp \tilde{I}_k\tilde{Z}_{ij} - V^i_{inj},$$

(15)

where $V^r_{i\alpha j}$ denotes the reflected voltage and $V^i_{i\alpha j}$ denotes the incident voltage and the upper and lower signs apply, respectively, for indexes

$$(i,j,k) \in \{(x,y,z),(y,z,x),(z,x,y)\}$$
and
$$(i,j,k) \in \{(x,z,y),(y,x,z),(z,y,x)\}.$$

(16)

To permit a simpler presentation in this paper, the derivation that follows only applies to the stub free mapped SCN where $Z_{sj} = Y_{oj} = R_{mj} = G_{ej} = 0$, and $Z_{ij} = Z_0$. However, the approach described can be straightforwardly applied to the general case of a stub loaded SCN node [16] and the hybrid SCN nodes.

Substituting the complex stretch factors (3) $S_i = 1 + \frac{\sigma_{si}}{j\omega}$, $S_k = 1 + \frac{\sigma_{sk}}{j\omega}$ into (13)

$$\tilde{V}_j(j\omega) = \frac{(j\omega+\sigma_{sk})\left(V^i_{inj}+V^i_{ipj}\right)+(j\omega+\sigma_{si})(V^i_{kpj}+V^i_{knj})}{2j\omega+\sigma_{sk}+\sigma_{si}}.$$

(17)

and applying the bilinear transformation [3] gives

$$\tilde{V}_j[z] = \alpha_j \begin{pmatrix} \frac{1}{2}\left(V^i_{inj}+V^i_{ipj}+V^i_{knj}+V^i_{kpj}\right) - \\ \frac{1}{2}\left(V^i_{inj}+V^i_{ipj}+V^i_{knj}+V^i_{kpj}\right)z^{-1} + \\ \frac{\sigma_{sk}\Delta t}{4}\left(\left(V^i_{inj}+V^i_{ipj}\right)+\left(V^i_{inj}+V^i_{ipj}\right)z^{-1}\right) + \\ \frac{\sigma_{si}\Delta t}{4}\left(\left(V^i_{knj}+V^i_{kpj}\right)+\left(V^i_{knj}+V^i_{kpj}\right)z^{-1}\right) + \\ \left(1-\frac{(\sigma_{si}+\sigma_{sk})\Delta t}{4}\right)\tilde{V}_jz^{-1} \end{pmatrix}$$
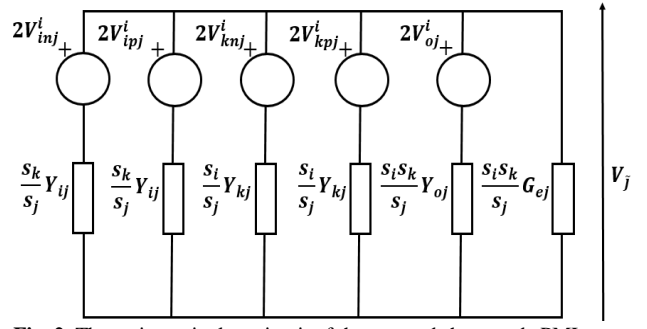
(18)

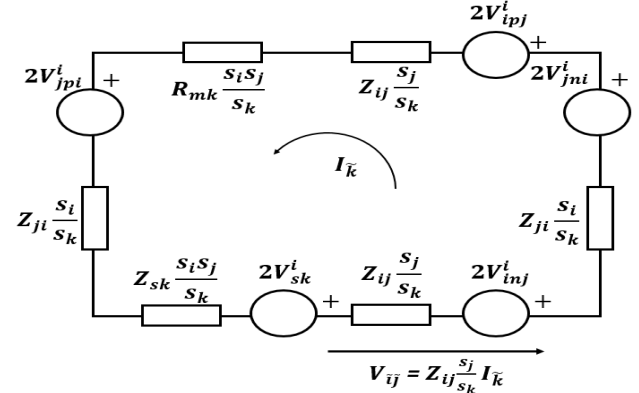**Fig. 2.** Thevenin equivalent circuit of the mapped shunt node PML.

Fig. 3. Thevenin equivalent circuit of the mapped series node PML.

where α_j is given by

$$\alpha_j = \frac{4}{4+(\sigma_{si}+\sigma_{sk})\Delta t},$$

(19)

To obtain a discrete time domain representation of $\tilde{V}_j[z]$ an inverse Z-transform is performed on (18), where z^{-1} indicates use of samples in the previous time step $(N-1)\Delta t$ and $N\Delta t$ denotes the current time step. This yields a compact formulation

$$_N\tilde{V}_j = \alpha_j \,_NV_j + \,_NV^{PML\_shunt}_j,$$

(20)

where $_NV_j$ represents the total voltage in the standard shunt circuit given as [2]

$$_NV_j = \frac{_NV^i_{inj}+\,_NV^i_{ipj}+\,_NV^i_{knj}+\,_NV^i_{kpj}}{2}$$

(21)

and $_NV^{PML\_shunt}_j$ represents the PML voltages attributed to $_N\tilde{V}_j$ and is given as

$$_NV^{PMLshunt}_j = $$

$$\alpha_j \begin{pmatrix} -\frac{1}{2}\,_{N-1}\left(V^i_{inj}+V^i_{ipj}+V^i_{knj}+V^i_{kpj}\right) + \\ \frac{\sigma_{sk}\Delta t}{4}\left(\,_N\left(V^i_{inj}+V^i_{ipj}\right)+\,_{N-1}\left(V^i_{inj}+V^i_{ipj}\right)\right) + \\ \frac{\sigma_{si}\Delta t}{4}\left(\,_N\left(V^i_{knj}+V^i_{kpj}\right)+\,_{N-1}\left(V^i_{knj}+V^i_{kpj}\right)\right) + \\ \left(1-\frac{(\sigma_{si}+\sigma_{sk})\Delta t}{4}\right)\,_{N-1}\tilde{V}_j \end{pmatrix}$$

(22)

Similarly, the discrete time form of the current $\tilde{I}_k$ is obtained by applying the bilinear transformation to (14) to yield

$$_N\tilde{I}_k = \alpha_k \left(\begin{array}{c} \left(_NI_k - {}_{N-1}I_k + \dfrac{\sigma_{sk}\Delta t}{2}(_NI_k + {}_{N-1}I_k) \right) + \\[2mm] \left(1 - \dfrac{(\sigma_{si} + \sigma_{sj})\Delta t}{4} \right) {}_{N-1}\tilde{I}_k \end{array} \right) \tag{23}$$

where $_NI_k$ represents the total k-directed current in the standard series circuit [2] given as

$$_NI_k = \frac{\left(_NV_{inj}^i - {}_NV_{ipj}^i \right) + \left(_NV_{kpj}^i - {}_NV_{knj}^i \right)}{2Z_0} \tag{24}$$

The total voltage $\tilde{V}_{ij}$ across the i-directed and j-polarized transmission line in the k-directed mapped series circuit (see Fig. 3) is given as

$$\tilde{V}_{ij} = \tilde{I}_k \tilde{Z}_{ij} = \tilde{I}_k Z_{ij} \frac{S_j}{S_k} \tag{25}$$

By applying the bilinear transformation to (25) a compact formulation for $\tilde{V}_{ij}$ is obtained as

$$_N\tilde{V}_{ij} = \alpha_k \, _NI_k Z_0 + {}_NV_{ij}^{PML\_series} \tag{26}$$

where $_NV_{ij}^{PML\_series}$ represents the PML voltages in the mapped series circuit given as

$$_NV_{ij}^{PML\_series} = \alpha_k \left(\begin{array}{c} Z_0 \left(-_{N-1}I_k + \dfrac{\sigma_{sj}\Delta t}{2}(_NI_k + {}_{N-1}I_k) \right) + \\[2mm] \left(1 - \dfrac{(\sigma_{si} + \sigma_{sj})\Delta t}{4} \right) {}_{N-1}\tilde{V}_{ij} \end{array} \right) \tag{27}$$

By substituting (26) and (20) into (15) the discrete time domain expression describing the scatter in the mapped SCN-PML is obtained. For example, the reflected voltage on the xnz transmission line is given as

$$_NV_{xnz}^r = \alpha_z \, _NV_z - \alpha_y \, _NI_y Z_0 - {}_NV_{xpz}^i + {}_NV_{xnz}^{PML} \tag{28}$$

where

$$_NV_{xnz}^{PML} = {}_NV_z^{PML\_shunt} - {}_NV_{xz}^{PML\_series} \tag{29}$$

In the connect phase of the TLM algorithm, the reflected voltages at the Nth time step become the incident voltages on neighboring nodes at the $(N+1)$ time step. In the standard TLM method with a real valued time step Δt, this results in a simple exchange of the pulses which is given for the xnz and xpz lines as

$$V_{xnz}^i (x + \Delta x, y, z, t) = V_{xpz}^r(x, y, z, t - \Delta t_x)$$

$$V_{xpz}^i(x - \Delta x, y, z, t) = V_{xnz}^r(x, y, z, t - \Delta t_x). \tag{30}$$

In the mapped SCN-PML, however, the time step is transformed to a complex variable as given in (9). The real part of the time step Δt_i is unchanged across each transmission line (*i.e.* $\Delta t = \Delta t_x = \Delta t_y = \Delta t_z$) ensuring that pulse synchronism is maintained across the SCN network. However, the imaginary component of Δt_i (9) introduces an attenuation in the transmission line modifying the connect equation, for example as

$$V_{xnz}^i (x + \Delta x, y, z, t) = V_{xpz}^r(x, y, z, t - \Delta t_x)e^{-\Delta t \sigma_{sx}}$$

$$V_{xpz}^i(x - \Delta x, y, z, t) = V_{xnz}^r(x, y, z, t - \Delta t_x)e^{-\Delta t \sigma_{sx}}. \tag{31}$$

In the mapped SCN-PML, control on the attenuation of the propagating fields is achieved by appropriately setting the values of σ_i. For a 'strong' PML, i.e. a high attenuating medium, the value of σ_i is increased to be much greater than zero.

III. THE MAPPED SCN-PML (12 PORT SCN)

Following the derivation made in section II the reflected pulses at each of the 12 ports of the mapped SCN-PML is summarized below,

$$\begin{aligned}
V_{ynx}^r &= \alpha_x V_x - \alpha_z I_z Z_0 - V_{ypx}^i + V_{ynx}^{PML} \\
V_{znx}^r &= \alpha_x V_x + \alpha_y I_y Z_0 - V_{zpx}^i + V_{znx}^{PML} \\
V_{xny}^r &= \alpha_y V_y + \alpha_z I_z Z_0 - V_{xpy}^i + V_{xny}^{PML} \\
V_{zny}^r &= \alpha_y V_y - \alpha_x I_x Z_0 - V_{zpy}^i + V_{zny}^{PML} \\
V_{ynz}^r &= \alpha_z V_z + \alpha_x I_x Z_0 - V_{ypz}^i + V_{ynz}^{PML} \\
V_{xnz}^r &= \alpha_z V_z - \alpha_y I_y Z_0 - V_{xpz}^i + V_{xnz}^{PML} \\
V_{ypz}^r &= \alpha_z V_z - \alpha_x I_x Z_0 - V_{ynz}^i + V_{ypz}^{PML} \\
V_{zpy}^r &= \alpha_y V_y + \alpha_x I_x Z_0 - V_{zny}^i + V_{zpy}^{PML} \\
V_{zpx}^r &= \alpha_x V_x - \alpha_y I_y Z_0 - V_{znx}^i + V_{zpx}^{PML} \\
V_{xpz}^r &= \alpha_z V_z + \alpha_y I_y Z_0 - V_{xnz}^i + V_{xpz}^{PML} \\
V_{xpy}^r &= \alpha_y V_y - \alpha_z I_z Z_0 - V_{xny}^i + V_{xpy}^{PML} \\
V_{ypx}^r &= \alpha_x V_x + \alpha_z I_z Z_0 - V_{ynx}^i + V_{ypx}^{PML}
\end{aligned} \tag{32}$$

with

$$\alpha_x = \frac{4}{4 + (\sigma_{sz} + \sigma_{sy})\Delta t} \quad , \quad \alpha_y = \frac{4}{4 + (\sigma_{sz} + \sigma_{sx})\Delta t}$$

$$\alpha_z = \frac{4}{4 + (\sigma_{sx} + \sigma_{sy})\Delta t}$$

where V_x, V_y and V_z denote the total x, y and z-directed voltages in the standard SCN node, respectively, and I_x, I_y and I_z denote the total currents flowing in the x, y and z-directions in the standard SCN node, respectively [2]. The voltages $V_{i\alpha j}^{PML}$

represent the PML voltages associated with the reflected pulses on each TL which are given as

$$V_{ynx,ypx}^{PML} = V_x^{PML\_shunt} \mp V_{yx}^{PML\_series}$$
$$V_{znx,zpx}^{PML} = V_x^{PML\_shunt} \pm V_{zx}^{PML\_series}$$
$$V_{xny,xpy}^{PML} = V_y^{PML\_shunt} \pm V_{xy}^{PML\_series}$$
$$V_{zny,zpy}^{PML} = V_y^{PML\_shunt} \mp V_{zy}^{PML\_series}$$
$$V_{ynz,ypz}^{PML} = V_z^{PML\_shunt} \pm V_{yz}^{PML\_series}$$
$$V_{xnz,xpz}^{PML} = V_z^{PML\_shunt} \mp V_{xz}^{PML_{series}}$$

$$(33)$$

where the upper sign, for example in component $V_{A,B}^{PML}$, is applied to line A and the lower sign is applied to the line B.

Note that for the case where $\sigma_i = \sigma_j = \sigma_k = 0$ then $V_j^{PML\_shunt} = V_{ij}^{PML\_series} = V_{i\alpha j}^{PML} = 0$ and $\alpha_i = \alpha_j = \alpha_k = 1$ and the above becomes the standard SCN TLM scatter equations [17]-[18] for a simple medium.

In the mapped SCN-PML the TLM synchronism criterion is maintained and the connect algorithm is modified by a applying a scaling along each TL direction. The modified connect equation is given as

$$_N V_{ynx}^i (x, y + \Delta y, z) = {}_{N-1}V_{ypx}^r(x, y, z)e^{-\sigma_{sy}\Delta t}$$
$$_N V_{znx}^i (x, y, z + \Delta z) = {}_{N-1}V_{zpx}^r(x, y, z)e^{-\sigma_{sz}\Delta t}$$
$$_N V_{xny}^i (x + \Delta x, y, z) = {}_{N-1}V_{xpy}^r(x, y, z)e^{-\sigma_{sx}\Delta t}$$
$$_N V_{zny}^i (x, y, z + \Delta z) = {}_{N-1}V_{zpy}^r(x, y, z)e^{-\sigma_{sz}\Delta t}$$
$$_N V_{ynz}^i (x, y + \Delta y, z) = {}_{N-1}V_{ypz}^r(x, y, z)e^{-\sigma_{sy}\Delta t}$$
$$_N V_{xnz}^i (x + \Delta x, y, z) = {}_{N-1}V_{xpz}^r(x, y, z)e^{-\sigma_{sx}\Delta t}$$
$$_N V_{ypz}^i (x, y - \Delta y, z) = {}_{N-1}V_{ynz}^r(x, y, z)e^{-\sigma_{sy}\Delta t}$$
$$_N V_{zpy}^i (x, y, z - \Delta z) = {}_{N-1}V_{zny}^r(x, y, z)e^{-\sigma_{sz}\Delta t}$$
$$_N V_{zpx}^i (x, y, z - \Delta z) = {}_{N-1}V_{znx}^r(x, y, z)e^{-\sigma_{sz}\Delta t}$$
$$_N V_{xpz}^i (x - \Delta x, y, z) = {}_{N-1}V_{xnz}^r(x, y, z)e^{-\sigma_{sx}\Delta t}$$
$$_N V_{xpy}^i (x - \Delta x, y, z) = {}_{N-1}V_{xny}^r(x, y, z)e^{-\sigma_{sx}\Delta t}$$
$$_N V_{ypx}^i (x, y - \Delta y, z) = {}_{N-1}V_{ynx}^r(x, y, z)e^{-\sigma_{sy}\Delta t}$$
$$. \qquad (34)$$

IV. NUMERICAL EXPERIMENTS

In this section the accuracy and stability of the developed method are demonstrated through various applications. As a reliable and benchmarkable test case, the canonical rectangular metal waveguide example is first demonstrated since a wide range of incidence angles can be achieved and performance comparisons can be made with other schemes. As an extended demonstration, an application involving the termination of materially inhomogeneous media is also presented where the numerical errors generated are demonstrated.

1) Absorption Performance

The reflection performance was investigated for an empty rectangular waveguide WR-28 of dimensions 7.116 mm by 3.556 mm by 12 mm ($\Delta l = 0.19$ mm) truncated by a 25 layer PML with parabolic conductivity grading and with a peak

conductivity of $\sigma_{max} = 25 \, S/m$. The PML layer was backed by a perfect electrical conductor (PEC). The excitation was the dominant TE_{10} mode profile amplitude modulated by a Gaussian pulse of center frequency 35.5 GHz and a bandwidth of 12 GHz. The plane of excitation was located at one node from the PML-waveguide interface and the observation node was set at the other end of the waveguide – one node away from the PML. The reflection coefficient was computed using a reference solution obtained from a simulation of a longer waveguide with dimensions (7.116 mm by 3.556 mm by 90 mm) terminated with PMLs after 600 time steps. The geometry of both waveguides is illustrated in Fig. 4. Figure 5 compares the reflection from the mapped SCN-PML with the SCN-PMLs presented in [9] and [10] and against the simple matched termination [2]. It can be seen that all the PML formulations offer substantial absorption (>40 dB) compared to the matched termination. However, while the new mapped SCN-PML only yields a reflection coefficient that is slightly better over much of the bandwidth, the next subsection will demonstrate why in practice it proves a far superior choice.
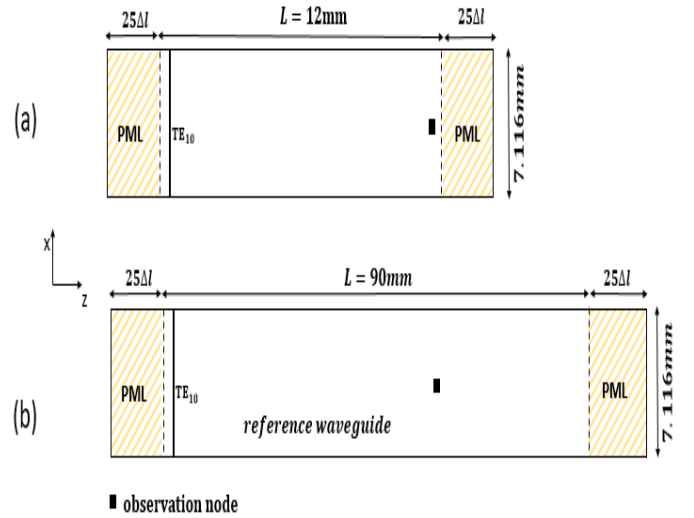

Fig. 4. Geometry of the simulated waveguide WR-28 truncated by PML with $25\Delta l$ ($\Delta l = 0.19 \, mm$) thickness: (a) test waveguide (b) reference waveguide.
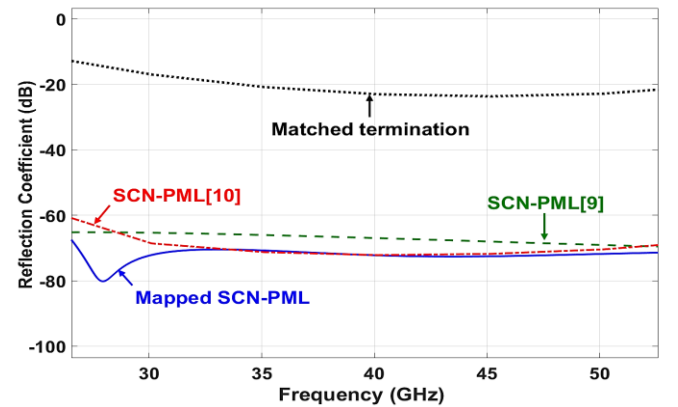

Fig. 5. Reflection coefficients obtained from a TLM simulated empty rectangular waveguide WR-28 truncated with parabolic graded $\sigma_{max} = 25 \, S/m$ $25\Delta l$ PML.
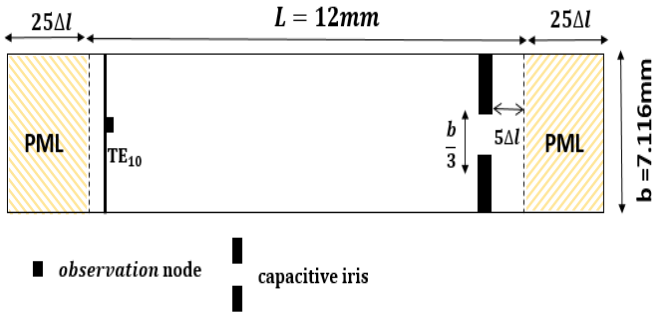
Fig. 6. Geometry of the rectangular waveguide WR-28 loaded with capacitive iris.

2) Stability

Stability is a critical requirement of all numerical time domain methods. To investigate the stability of the mapped SCN-PML the waveguide in Fig.4 was loaded with a capacitive iris of dimensions illustrated in Fig.6. The iris was placed close to the PML (5 nodes away) to ensure strong evanescent energy coupling with the PML interface. A strong 25 layer PML was employed by setting the peak conductivity to $\sigma_{max} = 48 \, S/m$ which was backed by a matched boundary condition. The observation and excitation were made at the same node at the opposite ends of the waveguide. The simulation set up was identical to that reported in [8] to allow for a wider comparison of TLM-PML schemes. The time domain plot of the E_y component is presented in Fig. 7 which is compared with the results using the SCN-PMLs [9] and [10]. As shown, instabilities arise when employing both [9] and [10]. We observed that the temporal behavior of the PML formulation proposed by [10] can be improved by setting the damping factor F >1, although this detrimentally increases the unphysical reflection from the PML, and typically instabilities still occur after ~30,000 time steps. The mapped SCN-PML is shown to exhibit no instability even with the iris placed at very close proximity to the PML. This demonstrates a substantial improvement in the temporal performance over existing SCN-PML schemes simulated in a similar context [7]-[11] which is regarded as the major advantage of the mapped SCN-PML scheme and hence contribution of this paper.
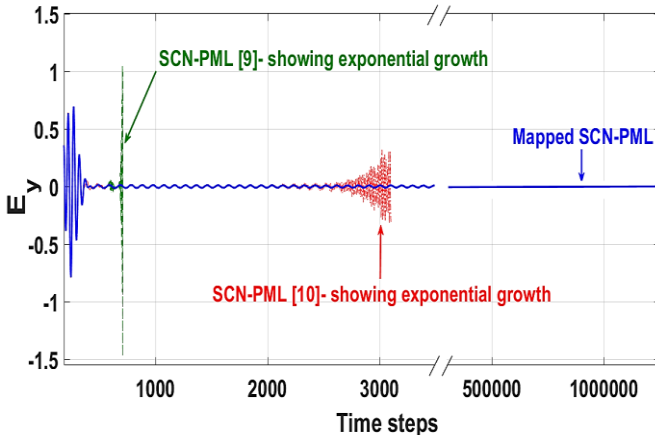

Fig. 7. Time domain waveform of an empty waveguide WR-28 loaded with a capacitive iris and truncated by different TLM-PMLs terminated by a matched boundary condition.

Next, an additional stability test was carried out to examine the response of the mapped SCN-PML to waves impinged on the layer for long durations of time. A practical application where such behavior is observed is in problems involving high quality-factor radiating structures. Since this test is solely focused on examining the time domain response, an electric dipole oscillating at 1 GHz with a very narrow bandwidth was used to inject energy into a cubic volume. The dipole source was placed at the center of a 11 mm × 11 mm × 11 mm uniformly meshed grid with $\Delta l = 1 \, mm$. All edges of the domain were surrounded by strong single PML layers with $\sigma_{x,y,z} = 18 \, S/m$ which were backed by a PEC boundary conditions. The observation point was set at a node two cells away from the cube corner. The normalized electric field obtained in the time domain from simulations employing the mapped SCN-PML is shown in Fig. 8 which is superimposed on an analytical time solution of a Hertzian dipole [19]. Results obtained from the SCN-PML schemes in [9] and [10] demonstrated instabilities very early on (before 1500 time steps) and have not been included in the plot. Fig.8 shows that results obtained with mapped SCN-PML implementation are in excellent agreement with the reference result and no instabilities are observed. For the given PML parameters we observed reflection errors lower than -65 dB. This simple test case is additionally important because it demonstrates the mapped SCN-PML stability in problems requiring a PML overlap i.e. in the corner region for which the previously published SCN-PML schemes are drastically unstable even in the absence of discontinuities in the domain.
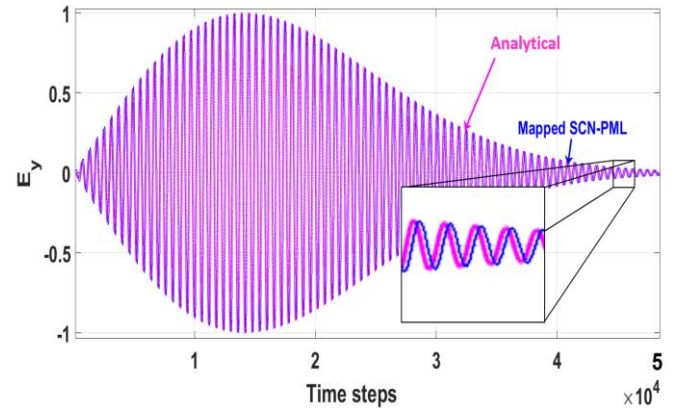

Fig. 8. Normalized E_y field obtained in the time domain from a narrow bandwidth dipole electric source with the mapped SCN-PML terminating the domain.

3) Inhomogeneous Media

Finally, as an extended demonstration, the accuracy and stability of the developed method in terminating materially inhomogeneous domains was evaluated. The field penetration through an infinitely extended substrate was considered as a suitable test since this offers a simple demonstration for problems where the inhomogeneity in the physical domain overlaps into the PML medium. The material parameters of the substrate were chosen to represent the effective material properties of a composite structure (as reported in [20]) and are given as: $\epsilon_{ry} = 2$, $\sigma_{ey} = 10000 \, Sm^{-1}$. At best when modeling lossy media the split-field based SCN-PMLs proposed in [9] and [10] can only be applied to cases with

isotropic losses i.e. $\sigma_{ex} = \sigma_{ey} = \sigma_{ez}$ as such these schemes cannot be applied to the above test case. A 3mm thick slab was placed (see inset Fig. 9.) at the middle of the computational domain whose dimension was set as 10 mm x 10 mm x 10 mm. The mesh discretization was set to $dl = 0.3$ mm. A four layer parabolic graded PML with $\sigma_{max_{x,y,z}} = 23\ S/m$ was applied on each face of the computational domain where the infinite extent of the substrate was simulated by overlapping the material properties of the slab into the PMLs on the x and z axis.

In this test, the problem domain was discretized using the Type I Hybrid symmetrical condensed node (HSCN $_I$) [21] which models both free space and inhomogeneous media. In the HSCN $_I$, the required inductances are modelled in the transmission lines, as such this alleviates the need for short circuit stubs and thus $Z_{sj} = 0$. For an anisotropic medium with diagonal tensors the characteristic impedances of the TL are now given as defined in [21],[22] therefore $Z_{ij} = Z_{ji}$ and $Z_{ij} \neq Z_{ik} \neq Z_{jk}$. Open circuit stubs are used to make up any deficit in capacitances and the node characteristic admittances Y_{oj} are defined for isotropic and anisotropic media as described in [21] , [22]. In the PML region the mapped approach developed in this paper was extended to the HSCN $_I$ to model the inhomogeneity in the PML region. Appropriate scatter equations for the mapped HSCN-PML are thus obtained by solving equations (13)-(15).

A 50 GHz differentiated Gaussian pulse was used as an excitation signal for the source which was placed 2 mm away from the slab. The transmitted fields were obtained 2 mm at the opposite side of the slab. The accuracy of the proposed method is compared against the matched termination in Fig. 9 where the error from both methods was computed as follows:

$$Error_{dB} = 20 \log 10\ (\left| E_y^t - E_{ref}^t \right|) \qquad (35)$$

where E_{ref}^t represents a reference solution which is the solution obtained by significantly extending the dimensions of the structure such that reflection effects from the boundaries are absent at the observation point. This therefore represents the *perfect* result. As shown, approx. 50 dB improvement is attained with the mapped HSCN-PML compared with the matched termination.

The shielding effectiveness of the substrate understudy is shown in Fig. 10, where the superior absorbing quality of the mapped HSCN-PML is demonstrated by the absence of oscillations in the results and the better convergence with the reference solution. In order to improve the convergence of the matched termination the computational domain would have to be significantly extended, therefore as expected the PML offers an improvement in computational efficiency in this manner.

Numerical instability was not observed in this investigation; therefore, further substantiating the utility of the proposed formulation.
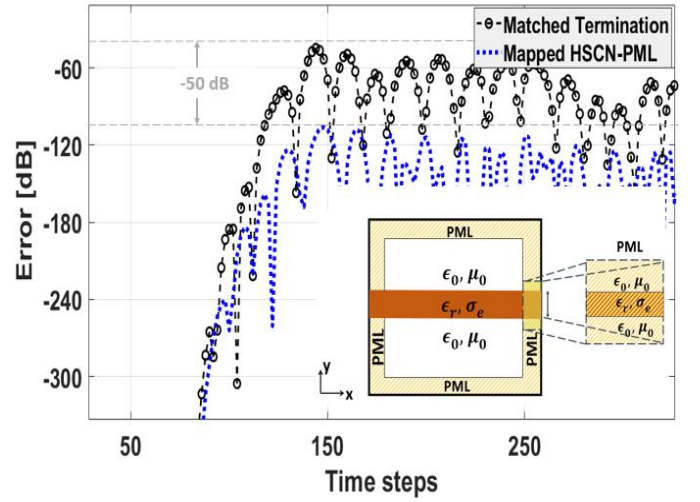

Fig. 9. Reflection errors in the time domain. Inset shows geometry of an infinitely extended lossy dielectric slab embedded in free space.
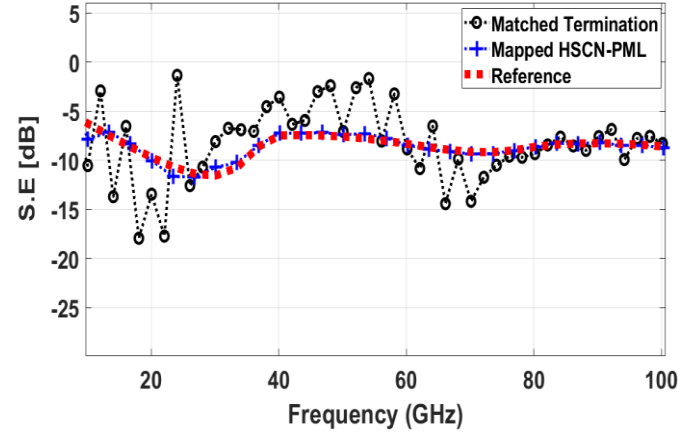

Fig. 10. Shielding effectiveness of an infinitely extended lossy dielectric slab embedded in free space.

V. CONCLUSIONS

Perfectly matched layers are critical to simulating large-scale electromagnetic problems. It is therefore highly desirable that PML implementations guarantee stability as well as high quality absorbing properties. An implementation that maps the unconditionally stable SCN to a complex stretched domain was demonstrated in this paper. This implements the PML theory by a transformation of the transmission line parameter which results in complex propagation delay, complex line admittances/impedances and modified scatter-connect equations. An improvement in absorption performance of the mapped SCN-PML implementation over earlier TLM-PML implementations is demonstrated. The scheme presented for the first time here demonstrates excellent temporal stability. Seeing that the underlying un-stretched SCN is provably unconditionally stable [1], this highly desired quality is shown to be preserved for the mapped SCN-PML since only the transmission line parameters are modified/stretched to achieve the required field attenuation. As such, this significantly extends the robustness of TLM-PML for realistic 3D simulations.

REFERENCES

[1] P. B. Johns, "A symmetrical condensed node for the TLM method," IEEE Trans. Microwave Theory Tech., vol. MTT-35, no. 4, pp. 370-377, Apr. 1987.

[2] C. Christopoulos, The Transmission-Line Modeling Method: TLM. IEE Press: Piscataway, NJ, 1995.

[3] J. Paul, C. Christopoulos, D.W.P. Thomas: Generalized material models in TLM – Part 1: Materials with frequency dependent properties, IEEE Trans. Ant. Prop., 50(7),pp. 997-1004, 1999.

[4] J. A. Morente, J. A. Porti, and M. Khalladi, "Absorbing boundary conditions for the TLM Method," IEEE Trans. Microwave Theory Tech., vol. 40, pp. 2095-2099, Nov. 1992.

[5] Z. Chen, M. M. Ney, and W. J. R. Hoefer, "Study of absorbing boundary conditions in the 3D-TLM symmetrical condensed node model," MTT Symp. Dig., Albuquerque, NM, pp. 369-372,1992.

[6] C. Eswarappa and W. J. R. Hoefer, "Implementation of Berenger's ́ absorbing boundary conditions in TLM by interfacing FDTD perfectly matched layers," Electron. Lett., vol. 31, no. 15, pp. 1264–1266, July 1995.

[7] N. Pena and M. M. Ney, "Absorbing-boundary conditions using perfectly matched layer (PML) technique for three-dimensional TLM simulations," IEEE Trans. Microwave Theory Tech., vol. 45, pp. 1749–1755, Oct. 1997.

[8] S. Le Maguer, N. Pena, and M. M. Ney, "Matched absorbing medium techniques for full-wave TLM simulation of microwave and millimeter-wave components, Ann. Telecommun., vol. 53, no. 3–4, pp. 115–129, Mar.–Apr. 1998.

[9] J. L Dubard, and D. Pompei "Optimization of the PML efficiency in 3-D TLM method." IEEE Transactions on Microwave Theory and Techniques; 48(7):1081–1087, 2000.

[10] L. Maguer, and M. M. Ney, "Extended PML-TLM node: an effcient approach for full waveanalysis of open structures." Int. J. Numer. Model., vol. 14 , pp. 129–144, 2001.

[11] T. W. Kang, C. Christopoulos, and J. Paul, "Implementation of the stretched co-ordinate-based PML for waveguide structures in TLM". International journal of numerical modelling electronic networks. Devices and fields. Vol. 18, pp. 107-118, 2005.

[12] J. Odeyemi, A. Vukovic, T. Benson, and P. Sewell, "An Improved PML implementation in the transmission line method." IET 10th International Conference on Computational Electromagnetics, 2019.

[13] J. P. Bérenger, "A perfectly matched layer for the absorption of electromagnetic waves," J. Comput. Phys., vol. 114, no. 1, pp. 185–200, 1994.

[14] W. C. Chew and W. H. Weedon, "A 3D perfectly matched medium from modified maxwell's equations with stretched coordinates," Microwave and Optical Tech. Lett., vol. 7, no. 13, pp. 599–604, 1994.

[15] A. J. Ward and J. B. Pendry, "Refraction and geometry in Maxwell's equations," J. Modern Optics, vol. 43, no. 4, pp. 773–793, 1996.

[16] V. Trenkic, C. Christopoulos, and T. M. Benson, "Development of a general symmetrical condensed node for the TLM method," IEEE Trans. Microwave Theory Tech., vol. 44, pp. 2129–2135, Dec. 1996.

[17] P. Naylor and R. Ait-Sadi, "Simple method for determining 3-D TLM nodal scattenng in nonscalar problems." Electron. Lett., vol. 28, no. 25, pp. 2353-2354, Dec. 1992.

[18] V. Trenkic, C. Christopoulos, and T. M. Benson, "Simple and elegant formulation of scattering in TLM nodes," Electron. Lett., vol. 29, no. 18, pp. 1651-1652, Sept. 1993.

[19] H.G. Schantz. "Electromagnetic energy around Hertzian dipoles." IEEE Ant. Prop. Magazine. vol.43, no,2, pp.50-62, 2001.

[20] M. S. Sarto, "A new model for the FDTD analysis of the shielding performances of thin composite structures," IEEE Transactions on Electromagnetic Compatibility, vol. 41, no. 4, pp. 298–306, 1999.

[21] R. A. Scaramuzza and A. J. Lowery, Hybrid symmetrical condensed node for TLM method", Electronics Letters, vol. 26, no.23, pp. 1947{1949, Nov. 1990.

[22] P. Berrini and K. Wu, A pair of hybrid symmetrical condensed TLM nodes", IEEE Microwave and Guided Wave Letters, vol. 4, no. 7, pp. 244{246, July 1994.

Jomiloju S. Odeyemi was born in Ibadan, Nigeria, in 1992. He received a First-class honors degree in electronic and electrical engineering from the University of Nottingham, Nottingham, U.K, in 2017. He is currently pursuing the Ph.D. degree in electrical and electronics engineering at the University of Nottingham, Nottingham, U.K. His current research interests are in numerical modelling of electromagnetics wave phenomena and improving the computational efficiency of CEM simulations.

Ana Vukovic (M'97) was born in Nis, Serbia, in 1968. She received the Diploma of Engineering degree in electronics and telecommunications from the University of Nis, Nis, Yugoslavia, in 1992, and the Ph.D. degree from the University of Nottingham, Nottingham, U.K., in 2000. From 1992 to 2001, she was a Research Associate with the University of Nottingham. In 2001, she joined the School of Electrical and Electronic Engineering, University of Nottingham, as a Lecturer. Her research interests are electromagnetics with a particular emphasis on applications in optoelectronics, microwaves, EMC and aerospace.

Trevor M. Benson received a First Class honors degree in Physics and the Clark Prize in Experimental Physics from the University of Sheffield in 1979, a PhD in Electronic and Electrical Engineering from the same University in 1982 and the DSc degree from the University of Nottingham in 2005. After spending over six years as a Lecturer at University College Cardiff, Professor Benson moved to The University of Nottingham in 1989. He was promoted to a Chair in Optoelectronics in 1996, having previously been Senior Lecturer (1989) and Reader (1994). Professor Benson's research interests include experimental and numerical studies of electromagnetic fields and waves with particular emphasis on the theory, modeling and simulation of optical waveguides, lasers and amplifiers, nano-scale photonic circuits and electromagnetic compatibility.

He is a Fellow of the Institute of Engineering Technology (FIET), the Institute of Physics (FInst.P) and the European

Optical Society (FEOS). He was elected a Fellow of the Royal Academy of Engineering in 2005 for his achievements in the development of versatile design software used to analyze propagation in optoelectronic waveguides and photonic integrated circuits.

Phillip D. Sewell was born in London, U.K., in 1965. He received the B.Sc. degree in electrical and electronic engineering (with first-class honors) and Ph.D. degree from the University of Bath, Bath, U.K., in 1988 and 1991, respectively. From 1991 to 1993, he was a Post-Doctoral Fellow with the University of Ancona, Ancona, Italy. In 1993, he became a Lecturer with the School of Electrical and Electronic Engineering, University of Nottingham, Nottingham, U.K. In 2001 and 2005, he became a Reader and Professor of electromagnetics at the University of Nottingham. His research interests involve analytical and numerical modeling of electromagnetic problems with application to opto-electronics, microwaves and aerospace applications.